Advanced Materials

ADVANCED MATERIALS
www.advmat.de

RESEARCH ARTICLE

Broadband Circularly Polarized Light Detection via Spin-Selective Charge Transport in Quantum Dot Photodiodes

Minseo Kim[1] | Shi Li[1] | Kyunghoon Lee[1] | Eonhyoung Ahn[1] | Soyeon Lee[1] | Kiwook Kim[1] | Hang Kim[1] | Wookyung Yu[2] | Changsoon Choi[3] | Jung Ah Lim[4,5] | Jeeseong Hwang[6] | Dae-Hyeong Kim[7,8] | Jiwoong Yang[1,9]

[1]Department of Energy Science and Engineering, Daegu Gyeongbuk Institute of Science and Technology (DGIST), Daegu, Republic of Korea | [2]Department of Brain Sciences, Daegu Gyeongbuk Institute of Science and Technology (DGIST), Daegu, Republic of Korea | [3]Center of Quantum Technology, Post-silicon Semiconductor Institute, Korea Institute of Science and Technology (KIST), Seoul, Republic of Korea | [4]Center of Electronic and Hybrid Materials Research, Korea Institute of Science and Technology (KIST), Seoul, Republic of Korea | [5]Department of Materials Science and Engineering, YU-KIST Institute Yonsei University, Seoul, Republic of Korea | [6]Applied Physics Division, National Institute of Standards and Technology, Boulder, Colorado, USA | [7]Center for Nanoparticle Research, Institute for Basic Science (IBS), Seoul, Republic of Korea | [8]School of Chemical and Biological Engineering, Institute of Chemical Processes, Seoul National University, Seoul, Republic of Korea | [9]Energy Science and Engineering Research Center, Daegu Gyeongbuk Institute of Science and Technology (DGIST), Daegu, Republic of Korea

Correspondence: Jiwoong Yang (jiwoongyang@dgist.ac.kr)

Received: 28 September 2025 | **Revised:** 9 December 2025 | **Accepted:** 14 January 2026

Keywords: broadband optoelectronics | chiral-induced spin selectivity | circularly polarized light detection | quantum dot photodiodes | spin-selective charge transport

ABSTRACT

Circularly polarized light (CPL) detection provides polarization-resolved information, enabling advanced applications in quantum technologies, bioimaging, secure communications, and multi-level optical data processing. However, conventional CPL photodetectors typically rely on intrinsically chiral absorbers, restricting operation to the UV–vis range and hindering extension into the near-infrared (NIR) and shortwave infrared (SWIR), which are critical for deep tissue imaging and low-visibility sensing. Here, we demonstrate broadband CPL detection with quantum dot (QD) photodiodes that exploit the chiral-induced spin selectivity effect in chiral-ZnO charge transport layers. Chiral ligand-functionalized ZnO electron transport layers selectively transmit spin-polarized charge carriers from QDs, enabling CPL-specific photocurrent generation even in spectral regions without intrinsic chiral absorption. Heavy-metal-free Cu–In–Se QD-photodiodes exhibit outstanding specific detectivity (D^*) of 1.28×10^{12} Jones without external bias and broadband CPL detection (g_{Iph}: ~0.17 at 260 nm and ~0.13 at 780 nm), while PbS QD-devices extend CPL detection across 250–1700 nm (UV–Vis–NIR–SWIR) with superior performance (D^*: 1.45×10^{12} Jones). The chiral-transport-driven strategy offers fundamental insights into CPL photodetection and establishes a scalable and optically passive platform for broadband polarization-resolved optoelectronics.

1 | Introduction

Photodetectors capable of sensing the handedness of circularly polarized light (CPL), in addition to conventional intensity and wavelength sensing, have attracted growing attention for diverse applications, including biomedical diagnostics, optical communication, quantum cryptography, environmental sensing, security systems, and multi-level optical data processing [1–4]. CPL carries

spin angular momentum arising from the helical rotation of its electric field vector perpendicular to the propagation direction [5–9], and is classified into left-handed and right-handed helicities [10–13]. Conventional photodetectors based on silicon or GaAs inherently lack CPL sensitivity, requiring external polarization optics that increase system complexity, enlarge device size, and reduce overall detection efficiency [14]. A conventional approach for realizing CPL-sensitive photodetectors is to employ chiral materials as photoactive layers [5, 7, 15–19], because chiral materials, defined by their mirror asymmetry, intrinsically respond differently to left-handed circularly polarized (LCP) and right-handed circularly polarized (RCP) light through mechanisms such as circular dichroism [20–27].

Extending CPL detection to the near-infrared (NIR) and short-wave infrared (SWIR) regions [28–35] is highly attractive because of advantages such as deep tissue penetration, reduced scattering, and low-energy operation—features highly beneficial for biomedical imaging and low-visibility applications (e.g., night vision) [36–38]. However, progress has been limited by the lack of materials that exhibit both strong chiroptical activity and efficient NIR/SWIR photoresponse (Tables S1 and S2). Chiral perovskites exhibit excellent CPL sensitivity in the UV–vis range but often show limited infrared response [39–41]. Two-photon absorption has also been investigated, yet its reliance on high-intensity and wavelength-specific excitation restricts practical use [42, 43]. Chiral organic materials with NIR activity have been tested, but they often suffer from poor stability and slow response times [28, 44–47]. While chiroptical activity has also been introduced into inorganic quantum dots (QDs), including those with NIR bandgaps, through their surface functionalization with chiral ligands [48–50], their dispersion in polar solvents leads to significant integration challenges with conventional charge transport layers, as polar solvents can dissolve or damage these layers, causing interlayer mixing and loss of interface integrity. This results in substantial difficulties in incorporating chiral-QDs into typical multilayered photodiode architectures. As a result, their use has been largely restricted to low-performance photoconductors or phototransistors, which face severe integration challenges for image-sensor-level architectures [2, 51, 52].

Traditionally, CPL photodetectors have relied on the intrinsic chirality of light-absorbing layers, raising a fundamental question of whether the intrinsic optical chirality of light absorbers is essential for CPL sensitivity. Inspired by recent advances in spin light-emitting diodes (spin-LEDs) [53–55], we propose an alternative strategy by introducing chirality into charge transport layers, offering a practical yet largely unexplored approach for CPL photodetectors. This strategy exploits the chiral-induced spin selectivity (CISS) effect, a quantum phenomenon in which electrons transmitted through chiral structures preferentially adopt one spin orientation even without external magnetic fields [56–60], thereby enabling spin-selective carrier extraction. This offers significant advantages, including simplified device integration, broad material compatibility, and robust CPL sensitivity with various absorbers. Crucially, because this approach does not depend on wavelength-limited optical chirality, it provides a straightforward route to extend CPL detection into the NIR/SWIR regions, where conventional chiral photoactive materials are scarce or inefficient. This concept underpins the present work.

Herein, we report broadband CPL-sensitive QD-photodetectors exploiting the CISS effect in chiral-ZnO electron transport layers (ETLs) (Figure 1a). The structural asymmetry of chiral-ZnO nanoparticles enables preferential transmission of spin-polarized carriers while suppressing opposite spins, effectively functioning as a spin filter for polarization-sensitive photocurrent extraction. We fabricated photodiodes (Figure 1b) comprising a chiral-ZnO ETL, a QD-photoactive layer, and a poly(3,4-ethylenedioxythiophene):poly(styrenesulfonate) (PEDOT:PSS) hole transport layer (HTL). Self-powered photodiodes based on heavy-metal-free Cu–In–Se (CISe) QDs exhibit outstanding specific detectivity (D^*) reaching 1.28×10^{12} Jones at 0 V and notable photocurrent dissymmetry factors (g_{Iph}) of ~0.17 at 260 nm and ~0.13 at 780 nm, demonstrating effective broadband CPL sensitivity from UV–vis to NIR (Table S2). The multilayer device platform described here is extendable to other QD materials, providing versatile material compatibility and enabling CPL detection into the SWIR region with excellent device performance (D^*: 1.45×10^{12} Jones, g_{Iph}: ~0.2 at 260 nm and ~0.14 at 1550 nm at 0 V). These findings propose chiral charge transport layers as a generalizable platform for broadband CPL detection, providing a scalable and optically passive strategy for next-generation quantum information technologies, optical communications, and biomedical imaging.

2 | Results and Discussion

2.1 | Preparation and Characterization of Chiral-ZnO Nanoparticles

In this study, ZnO nanoparticles were selected as a model system for chiral charge transport materials in QD-photodiodes owing to their widespread use as ETLs in QD-based optoelectronic devices, attributable to their high electron mobility, favorable band alignment for efficient electron extraction from QDs, and solvent orthogonality allowing for multilayer device fabrication [61–63]. Pristine-ZnO nanoparticles were synthesized by modifying a previously reported method [63] and subsequently functionalized with *L*/*D*-cysteine via ligand exchange process (see Experimental Section) [64, 65]. Transmission electron microscopy (TEM) analysis confirms an average particle size of 2.9 nm (Figure 1c; Figure S1), sufficiently small to enable effective chirality induction via surface functionalization [66]. Further size-dependent chirality studies show that larger ZnO nanoparticles (e.g., 7 nm) exhibit weaker chirality due to reduced surface effect by chiral ligand passivation (Figure S2). Therefore, this study focuses primarily on 2.9 nm-sized ZnO nanoparticles for the subsequent investigations.

To understand the influence of cysteine coordination modes on the optical chirality of ZnO nanoparticles, the pH condition during the ligand exchange reaction was systematically varied. Cysteine possesses thiolate, amino, and carboxylate groups (Figure 1a), whose ionization states depend on solution pH, with pK_a values of 1.71 for —COOH, 8.27 for —SH, and 10.8 for $—NH_3^+$. Depending on its protonation state, cysteine is expected to coordinate to the surface Zn^{2+} ions of ZnO nanoparticles in monodentate, bidentate, or tridentate modes, significantly influencing the induced chirality. It has been reported that tridentate coordination is preferred in other II–VI nanocrystals

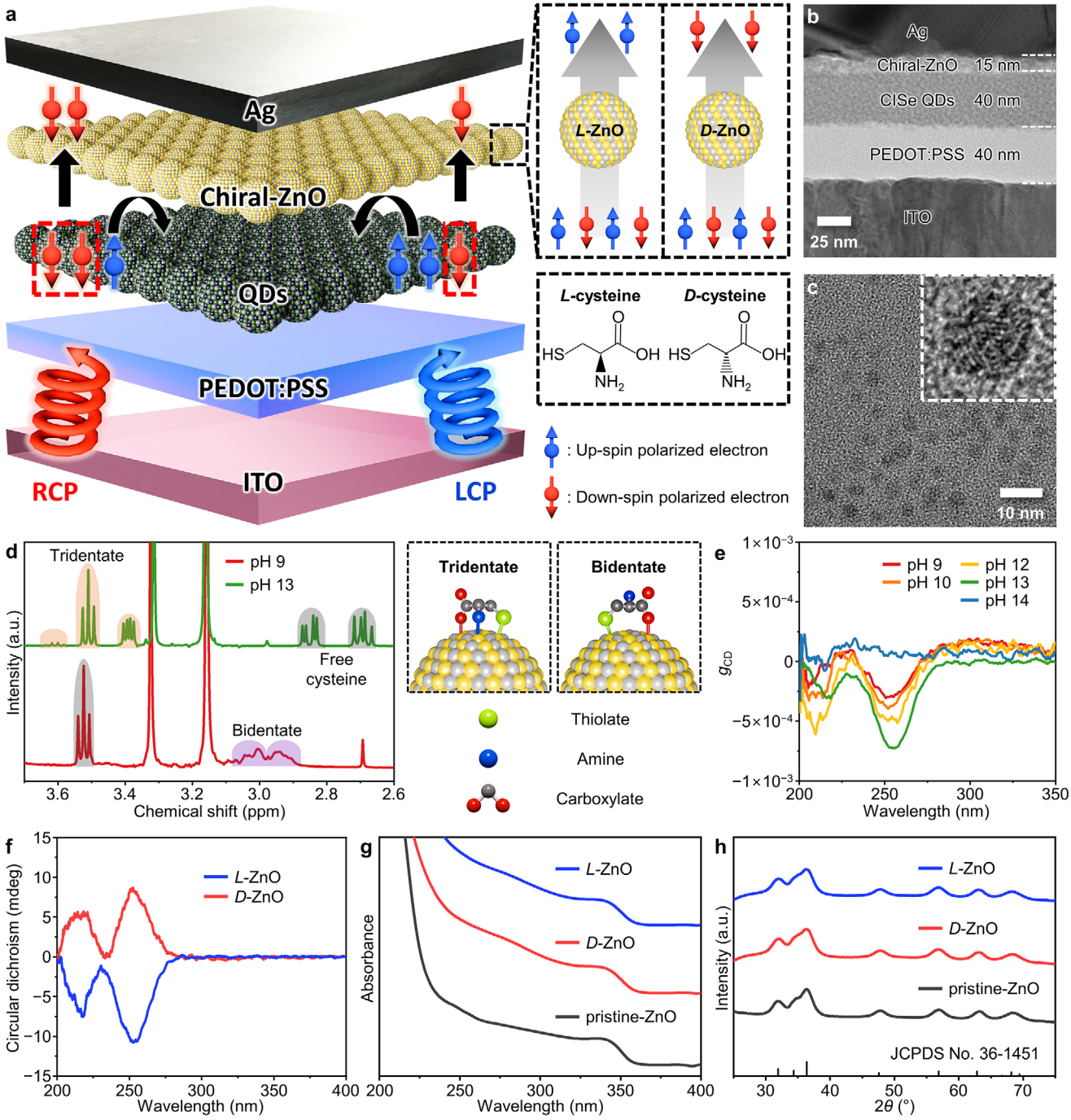

FIGURE 1 | Preparation and characterization of chiral-ZnO nanoparticles. (a) Schematic illustration of a QD-photodetector with a chiral charge transport layer. Cross-sectional TEM images of (b) CISe QD-photodetectors with chiral-ZnO ETL. (c) TEM image of chiral-ZnO nanoparticles. (d) ^{1}H NMR spectra of chiral-ZnO nanoparticles prepared at pH 9 and pH 13 during ligand exchange. (e) Circular dichroism spectra of *L*-ZnO nanoparticles prepared under different pH conditions, plotted as g_{CD}. (f) Circular dichroism spectra of *L*-ZnO and *D*-ZnO nanoparticles (pH 13). (g) Absorption spectra and (h) WAXS patterns of pristine-ZnO and chiral-ZnO nanoparticles.

because it imposes strong structural constraints, resulting in a rigid, non-rotational geometry that enhances chiral distortion compared to the more flexible bidentate binding mode [64].

^{1}H nuclear magnetic resonance (NMR) spectroscopy provides direct evidence of pH-dependent cysteine binding (Figure 1d). At high pH (12–13), cysteine proton signals exhibit clear downfield shifts (3.42 ppm, 3.50 ppm, and 3.63 ppm) relative to free cysteine, consistent with tridentate coordination involving thiolate, amino, and carboxylate groups. In contrast, at lower pH (9–10), below pK_a of the amino group, these signals are suppressed, and relative upfield peaks appear (3.05 ppm and 2.94 ppm), indicating bidentate binding [64]. Fourier-transform infrared (FT-IR) spectroscopy further supports this interpretation (Figure S3). Across all tested conditions (pH 9–13), the absence of the S—H stretching (~2550 cm^{-1}) and the presence of the COO^- bending

mode (801 cm^{-1}) confirm thiolate and carboxylate coordination. At pH 9–10, the amino groups remain protonated, as indicated by NH_3^+ rocking (1140 cm^{-1}) and asymmetric NH_3^+ stretching (3165 cm^{-1}), whereas at pH 12–13 these NH_3^+ peaks disappear and the NH_2 bending vibration emerges (3250 cm^{-1}) [67], indicating deprotonation and thus enabling tridentate binding.

The successful introduction of chirality in cysteine-capped ZnO nanoparticles was verified by circular dichroism spectroscopy. The anisotropy factor of circular dichroism (g_{CD}) reaches a maximum at pH 13, suggesting optimal cysteine-coordination as the tridentate mode (Figure 1e). *L*-cysteine-capped ZnO (*L*-ZnO) and *D*-cysteine-capped ZnO (*D*-ZnO) nanoparticles exhibit mirror-image circular dichroism signals with pronounced peaks at ~255 nm (Figure 1f), distinct from the characteristic circular dichroism spectra of free *L*/*D*-cysteine (Figure S4), implying strong interaction between cysteine and surface Zn^{2+} ions through ligand-to-metal charge transfer (LMCT) transitions [21, 68]. Absorption spectra of both *L*/*D*-ZnO nanoparticles resemble that of pristine-ZnO nanoparticles (Figure 1g), indicating the minimal alteration of the intrinsic band structure through cysteine-functionalization. Wide-angle X-ray scattering (WAXS, Figure 1h) and X-ray absorption near edge structure (XANES) analyses (Figure S5) reveal negligible changes between pristine- and chiral-ZnO nanoparticles, confirming the retention of the wurtzite crystal structure after the ligand exchange. X-ray photoelectron spectroscopy (XPS) further validates successful ligand exchange (Figure S6). The O 1s peak, originally consisting of lattice oxygen (530.1 eV) and surface-bound hydroxyl groups (531.0 eV), broadens and shifts toward higher binding energy (532.2 eV) after ligand exchange, consistent with the replacement of hydroxyl ligands by cysteine-derived carboxylates [69]. Additionally, the emergence of a clear S 2p [70] signal at 162 eV further confirms the presence of cysteine ligands on the ZnO surface.

2.2 | CISS Effect in the Chiral-ZnO ETLs

The CISS effect refers to the preferential transmission of charge carriers with a specific spin orientation through chiral materials [56–60]. To investigate spin-dependent charge transport in the chiral-ZnO ETLs, magnetic conductive-probe atomic force microscopy (mc-AFM) measurements were performed using magnetized probe tips. Prior to the measurements, the topographic uniformity of the chiral-ZnO film was confirmed by atomic force microscopy (AFM) imaging, ensuring reliable analysis of spin-polarized current generation. Notably, the chiral-ZnO ETLs can be uniformly deposited over wafer-scale areas (Figure S7), ensuring consistent spin-polarized current generation and suggesting their potential for large-scale image-sensor array production. Under applied bias, electrons flow from the sample to the magnetized probe tip, resulting in a measurable spin-polarized current. The spin polarization (P) of the transmitted electrons is calculated from the current–voltage (*I*–*V*) characteristics under two magnetization states (spin-up and spin-down) of the tip, using the following equation [71, 72]:

$$P = \frac{I_{spin-up} - I_{spin-down}}{I_{spin-up} + I_{spin-down}} \times 100\% \quad (1)$$

Initially, *I*–*V* characteristics of the chiral-ZnO films (thickness: 15 nm) on indium tin oxide (ITO) substrates were measured over 49 regions and averaged to ensure reproducibility (Figure 2a–c; Figure S8 and S9). *L*-ZnO films, which preferentially facilitate spin-up transport, exhibit significantly higher spin-up than spin-down currents, while the latter were lower than those measured using non-magnetized tips. Conversely, *D*-ZnO film, favoring transport of down-spin electrons, shows the opposite trend, with down-spin currents exceeding both spin-up and non-magnetized currents. The resulting spin polarization values of *L*-ZnO and *D*-ZnO are +85.2 ± 9.6% and −81.9 ± 8.84% at 2.0 V, respectively.

To further validate the CISS effect in practical devices, the same measurements were carried out on multilayer ITO/PEDOT:PSS/CISe QDs/chiral-ZnO structures (Figure 2d–f). As before, data from 50 different locations were averaged (Figure S10). Despite the reduced overall current due to the presence of the HTL and QD-photoactive layer, high spin polarization is still maintained, with values of +68% and −70% at 2.0 V for *L*-ZnO and *D*-ZnO, respectively, confirming the robustness of the CISS effect in actual device architectures.

The energy band structure of the chiral-ZnO nanoparticles was evaluated using cyclic voltammetry (CV) and Tauc plot analyses (Figure 2g; Figure S11), revealing the conduction band minimum (CBM) at −4.28 eV and the valence band maximum (VBM) at −7.77 eV. These values are consistent with the reported values for bulk ZnO (CBM = −4.2 eV and VBM = −7.5 eV) [73] with slight shifts attributed to dipole formation and trap passivation induced by cysteine functionalization [74, 75]. Mott–Schottky analysis further confirms their electrical properties, with the positive slopes indicating typical *n*-type semiconductor behavior (Figure 2h). The calculated carrier concentrations (*N*) for both *L*- and *D*-ZnO are comparable to those of pristine-ZnO nanoparticles (Figure 2i), indicating that cysteine functionalization does not alter the intrinsic *n*-type character or overall electronic properties.

2.3 | NIR CISe QD-Photodetectors with the Chiral-ZnO ETL

CISe QDs were selected as the photoactive material for QD-photodiodes owing to their strong broadband absorption from UV to NIR, excellent device performance [63, 76], and non-toxicity. Specifically, ~4 nm-sized CISe QDs were employed Figure 3a; see Supporting Information for experimental details based on our previous research, demonstrating their optimal performance in photodiode applications [63], particularly due to favorable band alignment. To enhance their electrical properties, the native long-chain oleylamine (OAm) ligands were replaced with shorter tetrabutylammonium iodide (TBAI) ligands via a solid-state ligand exchange process, confirmed by XPS (Figure S12). X-ray diffraction (XRD) reveals no structural changes after ligand exchange, retaining the tetragonal chalcopyrite phase (Figure S13). Ligand exchange induces a slight red-shift in the absorption band-edge from 1.38 eV to 1.36 eV (Figure 3b; Tauc plot in Figure S14), indicating enhanced electronic coupling between QDs due to reduced interparticle spacing. AFM imaging shows uniform surface morphology of the TBAI-CISe QD film on ITO without aggregation (Figure S15).

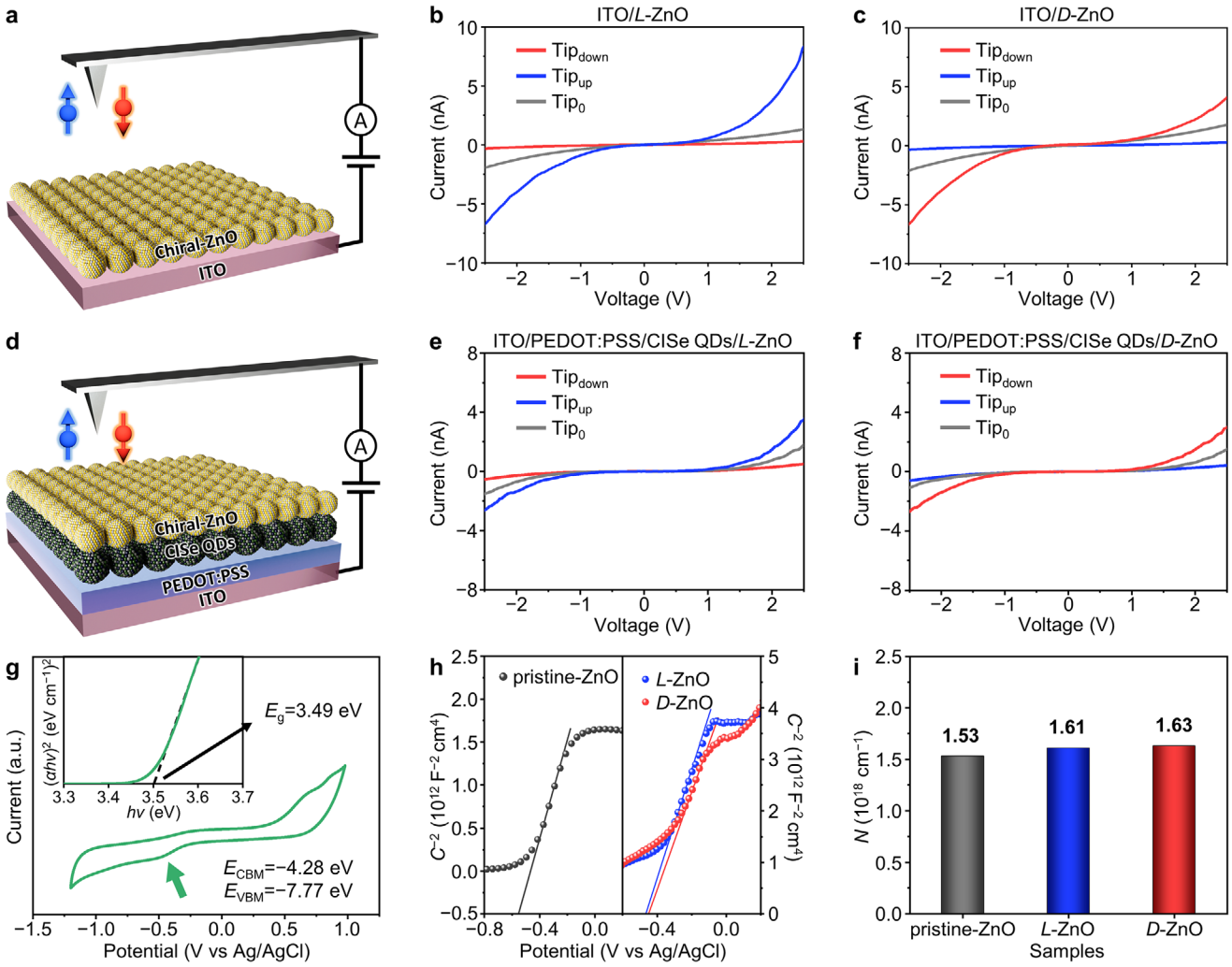

FIGURE 2 | CISS-driven spin transport and electrical properties of chiral-ZnO ETLs. (a) Schematic illustration of the mc-AFM measurement set-up for ITO/chiral-ZnO. *I–V* curves of (b) ITO/*L*-ZnO and (c) ITO/*D*-ZnO, measured with AFM tips under three magnetic states: non-magnetized (gray), magnetized up (blue), and magnetized down (red). (d) Schematic illustration of mc-AFM measurement set-up for ITO/PEDOT:PSS/CISe QDs/chiral-ZnO. *I–V* curves of (e) ITO/PEDOT:PSS/CISe QDs/*L*-ZnO and (f) ITO/PEDOT:PSS/CISe QDs/*D*-ZnO under three magnetic states: non-magnetized (gray), magnetized up (blue), and magnetized down (red). (g) CV curve and Tauc plot of *L*-ZnO nanoparticles. (h) Mott–Schottky plots of pristine-ZnO and chiral-ZnO nanoparticle films on a glassy carbon electrode measured at 10 kHz, and (i) estimated carrier concentrations.

QD-photodiodes with the multilayer structure of ITO/PEDOT:PSS (40 nm)/TBAI-CISe QDs (40 nm)/chiral-ZnO (15 nm)/Ag (90 nm) were fabricated for CPL detection. Cross-sectional TEM (Figure 1b) and EDS mapping (Figure S16) confirm the layer architecture and elemental distribution. The CPL measurement setup is depicted in Figure 3c, where RCP or LCP light is generated through a quarter-wave plate oriented at +45° or −45° relative to the light propagation axis, respectively. The energy band diagram for the device is illustrated in Figure 3d, with the energy levels of the CISe QDs determined by CV curves (Figure S17). Under the CPL illumination, spin-polarized electron–hole pairs are generated within the CISe QDs [2, 77], and charge carriers are separated by the built-in electric field: while holes migrate through the PEDOT:PSS HTL to ITO, spin-polarized electrons selectively pass through the chiral-ZnO ETL and move toward the Ag electrode, resulting in spin-dependent charge transport. The spin-polarized electron transport within the QD layer is supported by multiple mechanisms. First, the Rashba-type spin–orbit coupling arising from strong interfacial band bending (e.g., at the QD/ZnO junction) can lift spin degeneracy and reduce spin-flip scattering, thereby stabilizing non-equilibrium spin polarization during interfacial extraction [78]. Second, *n*-type doping (e.g., induced by TBAI passivation) generates excess free electrons, which are known to exhibit significantly longer spin lifetimes than excitonic carriers by avoiding fast electron–hole exchange interactions [79, 80]. Third, in the case of CISe QDs, intrinsic spatial separation between delocalized electrons and Cu-localized holes further suppresses spin relaxation by reducing wavefunction overlap [81]. The basic performance of the photodetectors was first evaluated under unpolarized illumination (see Supporting Information for experimental details). Current density–voltage (*J–V*) curves under dark and illumination conditions show clear rectifying behavior (Figure 3e). Due to the strong built-in potential, primarily originating from the Fermi-level offset between the QDs and ZnO-ETLs (Figure S18), the photodiodes operate effectively without external bias (i.e., self-powered operation), exhibiting broad spectral sensitivity from 250 to

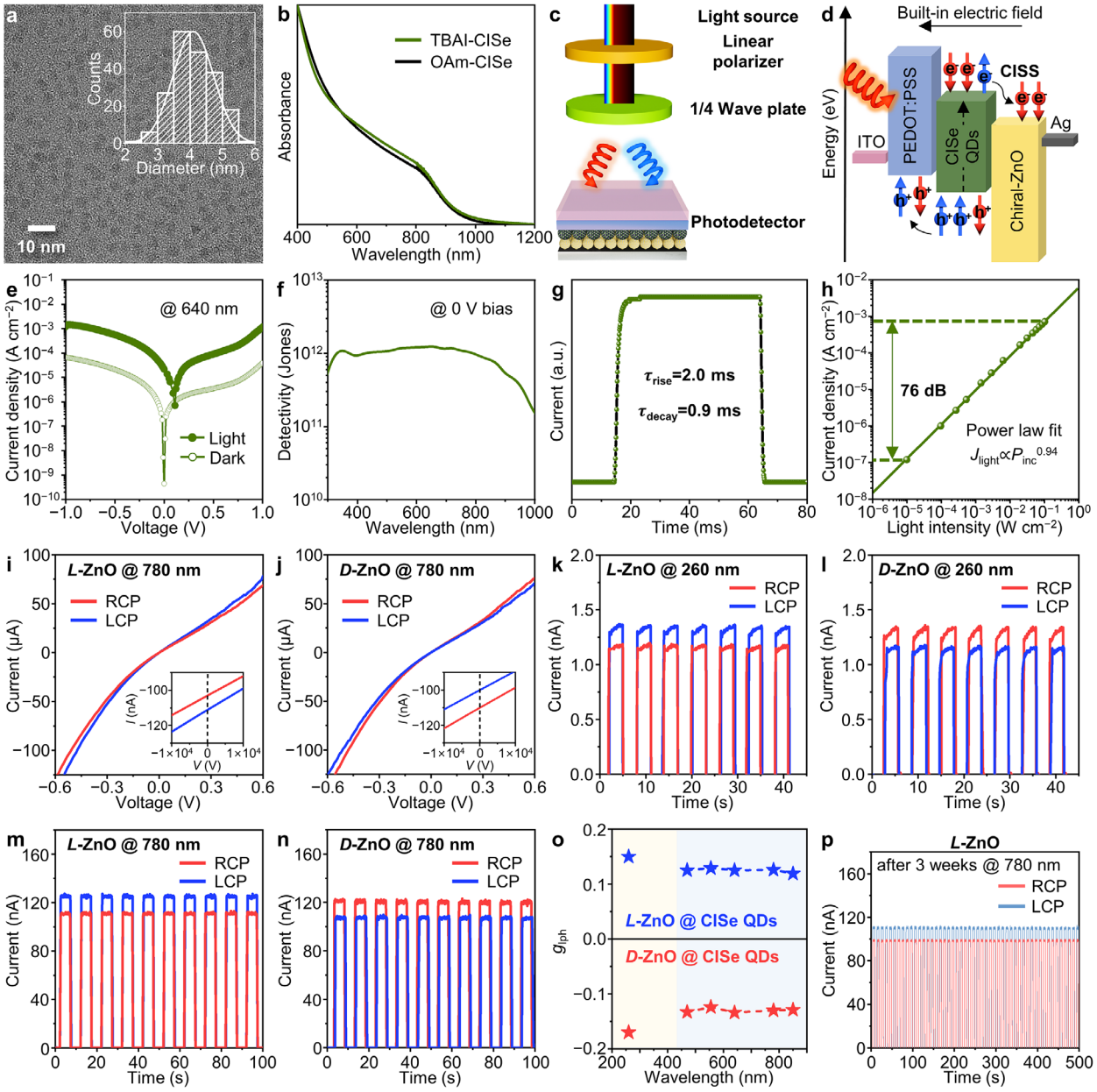

FIGURE 3 | UV–vis–NIR CPL detection of CISe QD-photodetectors with chiral-ZnO ETL. (a) TEM image of OAm-CISe QDs with size distribution histogram (average diameter: 4.1 ± 0.6 nm; n = 200). (b) Solid-state absorption spectra of OAm-CISe QD and TBAI-CISe QD films. (c) Schematic illustration showing the experimental setup. (d) Energy band diagram of CISe QD-photodiodes. (e) J–V characteristics of CISe QD-photodetectors with chiral-ZnO ETL under dark and illumination (640 nm, 5.1 mW cm^{-2}). (f) Wavelength-dependent D^* at 0 V bias. (g) Temporal photocurrent responses at 0 V bias (555 nm, 89 mW cm^{-2}). (h) LDR under 555 nm illumination (9.9 μW cm^{-2}–102 mW cm^{-2}). J–V curves of QD-photodetectors employing (i) L-ZnO and (j) D-ZnO ETL under LCP and RCP illumination (780 nm, 1.1 mW cm^{-2}). I–t curves of QD-photodetectors employing (k) L-ZnO and (l) D-ZnO ETL under 260 nm CPL illumination at 0 V bias. I–t curves of QD-photodetectors employing (m) L-ZnO and (n) D-ZnO ETL under 780 nm CPL illumination at 0 V bias. (o) Wavelength-dependent g_{Iph} at 0 V bias. p) I–t curves of L-ZnO ETL-based devices under CPL illumination (780 nm, 1.1 mW cm^{-2}). The device was remeasured after three weeks of storage following the initial test, demonstrating stability.

1000 nm. D^*, measured without external bias, exceeds 10^{12} Jones across the vis-to-NIR range (430–780 nm), with a peak of 1.28 × 10^{12} Jones at 640 nm (Figure 3f; Table S2). D^* was estimated from photocurrent responsivity (R_I) and noise current density (Figure S19), considering thermal and flicker noise beyond shot noise to avoid overestimation. Furthermore, our devices exhibit rapid responses (rise: 2.0 ms, decay: 0.9 ms; Figure 3g) and a wide linear dynamic range (LDR) of ~76 dB (9.9 μW cm^{-2}–102 mW cm^{-2}; Figure 3h). Overall, the devices show performance comparable to state-of-the-art heavy-metal-free QD-photodiodes [63].

To examine the limitations of incorporating chirality directly into QDs, photodetectors employing cysteine-capped CISe QDs as the photoactive layer were fabricated (see Supporting Information for experimental details). Cysteine-capped CISe QDs exhibit good dispersibility in polar solvents, complicating multilayer

fabrication due to interfacial mixing. This limits the device architecture to a simple photoconductor configuration without dedicated charge transport layers that are essential for the effective charge extraction from QDs. Consequently, device performances are notably inferior compared to devices utilizing the chiral-ZnO ETL, yielding over three orders of magnitude lower detectivity (Figure S20). This highlights the advantage of introducing chirality into charge transport layers rather than photoactive layers.

CPL discrimination without external polarization optics is clearly demonstrated, even at the wavelengths where the chiral-ZnO ETLs lack intrinsic optical chirality (Figure S21). For example, under 780 nm illumination, devices employing the *L*-ZnO ETL generate higher photocurrent under LCP illumination than RCP, whereas devices with the *D*-ZnO ETL exhibit the opposite trend (Figure 3i,j), consistent across the tested bias range. These results indicate that the observed CPL sensitivity arises from the CISS effect of the chiral-ZnO ETLs rather than from chiral optical absorption.

Current–time (*I*–*t*) measurements under repeated CPL on/off cycles at 0 V bias provide reliable quantification of photocurrent dissymmetry factors (g_{Iph}), which are calculated as follows [63]:

$$g_{Iph} = \frac{2\,(I_L - I_R)}{I_L + I_R} \tag{2}$$

where I_L and I_R represent the photocurrent generated under LCP and RCP illumination, respectively. g_{Iph} The devices employing the *L*-ZnO and *D*-ZnO ETL exhibit g_{Iph} values of +0.15 and −0.17 at 260 nm, demonstrating stable spin-dependent photoresponse over time (Figure 3k,l). At 780 nm, where the chiral-ZnO ETLs lack light absorption, g_{Iph} is ∼0.13 (Figure 3m,n). The reduced g_{Iph} at 780 nm compared to 260 nm is attributed to the absence of intrinsic optical chirality in the ETLs at this wavelength (Figure S22), implying that CPL discrimination originates solely from the CISS effect at 780 nm, whereas both CISS and optical chirality contribute at 260 nm. Measurements at additional wavelengths (470, 555, 640, and 850 nm) without light absorption by the chiral-ZnO ETLs yield similar g_{Iph} of ∼0.13 (Figure 3o; Figure S23), further confirming the proposed mechanism. Increasing the chiral-ZnO ETL enhances spin-selective photocurrent responses (Figure S24), consistent with previous findings [56]. In contrast, increasing the CISe QD thickness causes both D^* and g_{Iph} to decrease (Figure S25) due to enhanced scattering [82], further confirming the optimal QD thickness of 40 nm. No CPL response is observed in QD-photodetectors with the pristine-ZnO ETL (Figure S26). Long-term stability tests demonstrate negligible degradation in g_{Iph} after three weeks, confirming robust device stability (Figure 3p; Figure S27).

2.4 | SWIR QD-Photodetectors with the Chiral-ZnO ETL

For extended CPL detection into the SWIR regime, we developed QD-photodiodes by integrating the chiral-ZnO ETL with SWIR QDs. PbS QDs (∼6 nm in diameter), initially capped with oleic acid (OA), were synthesized via a colloidal hot-injection method (Figure 4a; see Supporting Information for experimental details) [83]. PbS QDs have long served as a model material system in the infrared QD research field due to their wide bandgap tunability from the NIR (∼1.0 μm) to the SWIR region (up to ∼2.5 μm) and excellent electrical properties [83]. The native long-chain OA ligands were replaced with TBAI through a solid-state ligand exchange process analogous to that used for CISe QDs, inducing a slight red-shift in absorption spectra (Figure 4b). Successful ligand exchange is confirmed by XPS (Figure S28), and XRD verifies retention of the PbS rock-salt crystal structure (Figure S29). SWIR-sensitive PbS QD-photodetectors with the chiral-ZnO ETL were fabricated with the architecture of ITO/PEDOT:PSS (30 nm)/TBAI-PbS QDs (100 nm)/chiral-ZnO (25 nm)/Ag (90 nm), consistent with the CISe devices except for the light absorber materials and layer thicknesses (Figure 4c). Energy levels and corresponding band alignments were determined using the Tauc plot and CV analyses (Figure S30). Similar to the case of CISe QDs, spin-polarized transport in the PbS QDs is also expected to be supported by the presence of excess free electrons [79, 80] introduced by the TBAI treatment and Rashba-type spin–orbit coupling [78] at the QDs/chiral-ZnO interface. These effects help preserve spin polarization during interfacial extraction, enabling CPL-resolved detection in the SWIR regime.

Basic device performance was evaluated under unpolarized illumination. *J*–*V* characteristics show clear rectifying behavior (Figure 4d), indicating self-powered operation without external bias, which is attributed to the strong built-in potential at QDs/ZnO interfaces (Figure S31). The devices exhibit broad spectral response from 250 nm to 1700 nm, with an outstanding maximum D^* of 1.45×10^{12} Jones at 1490 nm at 0 V bias (Figure 4e; Figure S32). Temporal responses are notably fast (rise time: 0.46 ms, decay time: 0.34 ms; Figure 4f) and *LDR* is 88 dB (Figure 4g), outperforming CISe QD-based devices. Overall, these QD-photodiodes deliver outstanding performance across UV–vis–NIR–SWIR, surpassing previously reported CPL-sensitive photodetectors [5, 7–9, 11, 15, 16, 22, 24, 25, 28, 29, 31–35, 42, 43, 56, 72, 84–86] (Table S2) and performing comparably to state-of-the-art, non-CPL-sensitive SWIR QD-photodiodes [87–92] (Table S3).

To assess CPL detection capability, *I*–*t* responses were recorded under repeated CPL on/off cycles at 0 V bias. PbS QD-photodetectors with the chiral-ZnO ETL exhibit clear photocurrent dissymmetry under CPL illumination across a wide spectral range (Figure 4h). At 260 nm, g_{Iph} reaches ∼0.2 (Figure 4i,j). To elucidate the role of the chiral-ZnO ETL as a spin-selective transport layer, additional measurements were conducted at the wavelengths lacking intrinsic circular dichroism (Figure S33). At 1550 nm, a representative SWIR wavelength, distinct g_{Iph} values (∼0.14) persist for both *L*-ZnO and *D*-ZnO-based devices (Figure 4k,l). Measurements at 470, 555, 640, and 850 nm give similar g_{Iph} (Figure S34). These results clearly demonstrate that the observed CPL sensitivity originates from spin-dependent charge transport through the chiral-ZnO ETLs, independent of the intrinsic optical chirality of the QD absorbers. Furthermore, varying the thickness of the PbS QD layer reveals that g_{Iph} increases as the layer becomes thinner, with the highest values of ∼0.23 observed at 45 nm due to minimized spin depolarization during transport (Figure S35). However, very thin films suffer from reduced optical absorption, leading to lower D^*. To ensure

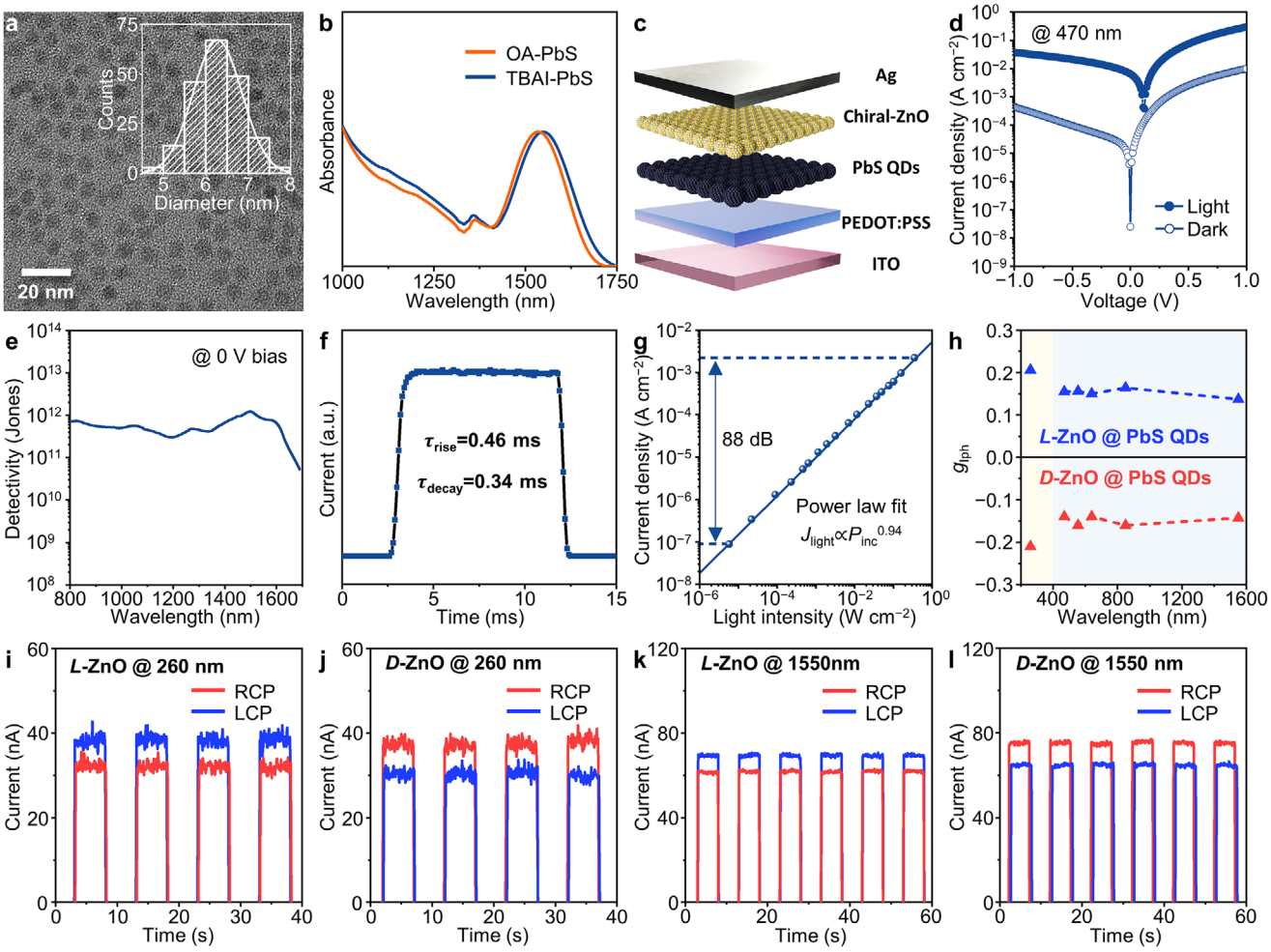

FIGURE 4 | UV–vis–NIR–SWIR CPL detection of PbS QD-photodetectors with chiral-ZnO ETL. (a) TEM image and size distribution histogram of PbS QDs (average diameter: 6.2 ± 0.5 nm; $n = 200$). (b) Solid-state absorption spectra of OA-PbS QD and TBAI-PbS QD films. (c) Schematic illustration showing the device structure of PbS QD-photodetectors. (d) Logarithmic *J*–*V* characteristics of PbS QD-photodetectors with chiral-ZnO ETL under dark and illumination (470 nm, 21 mW cm^{-2}). (e) Wavelength-dependent *D** at 0 V bias. (f) Temporal photocurrent responses at 0 V bias (555 nm, 89 mW cm^{-2}). (g) *LDR* under 555 nm illumination (5.7 μW cm^{-2}–127 mW cm^{-2}). (h) Wavelength-dependent g_{Iph} at 0 V bias. *I*–*t* curves of QD-photodetectors employing (i) *L*-ZnO and (j) *D*-ZnO ETL under 260 nm CPL illumination at 0 V bias. *I*–*t* curves of QD-photodetectors employing (k) *L*-ZnO and l) *D*-ZnO ETL under 1550 nm CPL illumination at 0 V bias.

both strong CPL selectivity and reliable photodetector performance, we therefore adopted a 100 nm-thick PbS QD layer as the optimized configuration. This thickness offers a practical balance between preserving spin polarization and achieving sufficient SWIR absorption.

3 | Conclusion

In this study, we have demonstrated broadband CPL-sensitive QD-photodetectors covering the UV–vis–NIR–SWIR range by integrating the chiral-ZnO ETL with NIR/SWIR QDs. By leveraging the CISS effect, the chiral-ZnO ETLs selectively transmit spin-polarized carriers generated in the QD-photoactive layers. This enables robust polarization-specific photocurrent responses across a wide spectral range, even beyond the intrinsic absorption of chiral-ZnO nanoparticles. Self-powered photodiodes based on heavy-metal-free CISe QDs exhibit outstanding *D** over 10^{12} Jones without external bias and broadband CPL sensitivity (g_{Iph}: ~0.17 at 260 nm, ~0.13 at 780 nm). Furthermore, PbS QD-based devices achieve superior device performance (*D**: 1.45 × 10^{12} Jones) with broadband CPL sensitivity spanning UV–vis–NIR–SWIR (g_{Iph}: ~0.2 at 260 nm and ~0.14 at 1550 nm). These results demonstrate that CPL detection capability does not necessarily require intrinsic optical chirality in photoactive materials. Instead, integrating chiral charge transport layers offers a powerful, generalizable, and scalable strategy for broadband CPL photodetection, significantly broadening the scope of polarization-sensitive optoelectronics across the UV–vis–NIR–SWIR spectrum.

4 | Experimental Section

4.1 | Chemicals and QD synthesis

Detailed information on the chemicals used and the synthesis procedures for QDs is described in the Supporting Information.

4.2 | Synthesis of pristine-ZnO nanoparticles

ZnO nanoparticles were synthesized following a modified version of our previously reported method [63]. Briefly, for the typical synthesis of ~3 nm-sized ZnO nanoparticles, 3.0 mmol of zinc acetate·$2H_2O$ was dissolved in 30.0 mL of dimethyl sulfoxide and stirred at 30°C for 1 h. Separately, 0.5 mmol of tetramethylammonium hydroxide was dissolved in 10.0 mL of ethanol. Then, the tetramethylammonium hydroxide solution was added dropwise into the zinc acetate solution at a controlled rate of 0.5 mL min^{-1} while maintaining vigorous stirring at 30°C for 1 h. The products were purified by centrifugation using ethyl acetate and finally re-dispersed in 1-propanol for subsequent experiments. Larger ZnO nanoparticles (~7 nm) were obtained by modifying only the reaction temperature and time (60°C for 3 h), while keeping all other conditions, including reagent concentrations, solvent compositions, and purification procedures, identical to the original synthesis.

4.3 | Functionalization of ZnO nanoparticles with chiral ligands

The functionalization of ZnO nanoparticles with chiral ligands was carried out by standard ligand exchange procedures [64, 93]. Briefly, 2.0 mL of a cysteine ligand solution (0.2 M in methanol) was mixed with an aqueous tetramethylammonium hydroxide solution (0.25 M) to adjust the pH to the desired value. Subsequently, 3.0 mL of a ZnO nanoparticle solution (1.23 M in 1-propanol, Zn basis) was added, followed by stirring for 30 min. The resulting nanoparticles were purified via centrifugation with acetone. After discarding the supernatant, the chiral-ZnO nanoparticles were re-dispersed in ethanol for further use.

4.4 | Fabrication of QD-photodiodes with the chiral-ZnO ETL

CISe QD-photodiodes were fabricated with a device architecture of ITO/PEDOT:PSS/TBAI-CISe QDs/chiral-ZnO/Ag. Initially, ITO substrates were sequentially cleaned with detergent and deionized water, followed by ultrasonication in acetone for 15 min. After drying, the substrates were exposed to UV-ozone for 30 min. A PEDOT:PSS layer was deposited via spin-coating (1000 rpm, 30 s) and subsequently annealed at 180°C for 20 min. A CISe QD-photoactive layer was prepared using a solid-state ligand exchange protocol. CISe QD dispersion in toluene was spin-coated (2000 rpm, 15 s), followed by the drop-casting of TBAI solution (10 mg mL^{-1} in ethanol) for 1 min. The film was then rinsed twice with ethanol to remove unbound ligands. This QD deposition and ligand-exchange cycle was repeated until the desired film thickness was achieved, followed by annealing at 100°C for 5 min. Subsequently, the chiral-ZnO ETL was spin-coated (2000 rpm, 15 s) from a chiral ZnO nanoparticle dispersion (0.74 M in ethanol) and annealed at 100°C for 10 min. Finally, a 90 nm Ag electrode was deposited by thermal evaporation. For the fabrication of PbS QD-photodiodes with the chiral-ZnO ETL, a similar procedure was followed, except the CISe QD solution was replaced with a PbS QD solution.

4.5 | NIST Disclaimer

Certain commercial materials and equipment are identified to adequately specify the experimental procedure. Such identification does not imply recommendation by the National Institute of Standards and Technology.

Acknowledgements

This work was supported by the Ministry of Trade, Industry, and Energy (MOTIE) and Korea Institute for Advancement of Technology (KIAT) through the International Cooperative R&D program (grant no. P0026257) and the National Research Foundation of Korea (NRF) grant funded by the Korea government (MSIT) (No. RS-2024-00406548). Experiments at PLS-II were supported in part by MSIT and POSTECH.

Conflicts of Interest

The authors declare no conflict of interest.

Data Availability Statement

The data that support the findings of this study are available in the supplementary material of this article.

References

1. E. Togan, Y. Chu, A. S. Trifonov, et al., "Quantum Entanglement Between an Optical Photon and a Solid-State Spin Qubit," *Nature* 466 (2010): 730, https://doi.org/10.1038/nature09256.

2. H. Al-Bustami, B. P. Bloom, A. Ziv, et al., "Optical Multilevel Spin Bit Device Using Chiral Quantum Dots," *Nano Letters* 20 (2020): 8675, https://doi.org/10.1021/acs.nanolett.0c03445.

3. Q. Wang, J. Bao, Y. Zhang, et al., "High-Performance Organic Narrow Dual-Band Circular Polarized Light Detection for Encrypted Communications and Color Imaging," *Advanced Materials* 36 (2024): 2312396, https://doi.org/10.1002/adma.202312396.

4. G. Jang, D.-Y. Jo, S. Ma, et al., "Core–Shell Perovskite Quantum Dots for Highly Selective Room-Temperature Spin Light-Emitting Diodes," *Advanced Materials* 36 (2024): 2309335, https://doi.org/10.1002/adma.202309335.

5. X. Zhang, Y. Xu, A. N. Alphenaar, et al., "Self-Powered Circularly Polarized Light Detection Enabled by Chiral Two-Dimensional Perovskites With Mixed Chiral–Achiral Organic Cations," *ACS Nano* 18 (2024): 14605, https://doi.org/10.1021/acsnano.4c02588.

6. C. He, Z. Tang, C. Wang, et al., "Gradient-Metasurface-Contact Photodetector for Visible-to-Near-Infrared Spin Light," *Advanced Materials* 37 (2025): 2418405, https://doi.org/10.1002/adma.202418405.

7. C. Chen, L. Gao, W. Gao, et al., "Circularly Polarized Light Detection Using Chiral Hybrid Perovskite," *Nature Communications* 10 (2019): 1927, https://doi.org/10.1038/s41467-019-09942-z.

8. L. Wang, Y. Xue, M. Cui, et al., "A Chiral Reduced-Dimension Perovskite for an Efficient Flexible Circularly Polarized Light Photodetector," *Angewandte Chemie International Edition* 59 (2020): 6442, https://doi.org/10.1002/anie.201915912.

9. Y. Zhao, Y. Qiu, J. Feng, et al., "Chiral 2D-Perovskite Nanowires for Stokes Photodetectors," *Journal of the American Chemical Society* 143 (2021): 8437, https://doi.org/10.1021/jacs.1c02675.

10. H.-Y. Hou, S. Tian, H.-R. Ge, J.-D. Chen, Y.-Q. Li, and J.-X. Tang, "Recent Progress of Polarization-Sensitive Perovskite Photodetectors," *Advanced Functional Materials* 32 (2022): 2209324, https://doi.org/10.1002/adfm.202209324.

11. H. Kim, W. Choi, Y. J. Kim, et al., "Giant Chiral Amplification of Chiral 2D Perovskites via Dynamic Crystal Reconstruction," *Science Advances* 10 (2024): ado5942.

12. Y. Kim, J. Lee, W.-H. Yeo, et al., "Rapid Polarization-Controlled Depth Sensing and Imaging with an Electrically Tunable Metalens," *Nano Letters* 25 (2025): 9394, https://doi.org/10.1021/acs.nanolett.5c01831.

13. Y. Li, L. Jiang, J. Tang, et al., "Unraveling Chiral Perovskite Spin-Light Emitting Diode Performance and Magneto-Chiroptical Properties Relationship Due to the Synergistic Effect," *Advanced Functional Materials* 35 (2025): 2424619, https://doi.org/10.1002/adfm.202424619.

14. W. R. Kitzmann, J. Freudenthal, A.-P. M. Reponen, Z. A. VanOrman, and S. Feldmann, "Fundamentals, Advances, and Artifacts in Circularly Polarized Luminescence (CPL) Spectroscopy," *Advanced Materials* 35 (2023): 2302279, https://doi.org/10.1002/adma.202302279.

15. A. Ishii and T. Miyasaka, "Direct Detection of Circular Polarized Light in Helical 1D Perovskite-Based Photodiode," *Science Advances* 6 (2020): abd3274.

16. Z. Liu, C. Zhang, X. Liu, et al., "Chiral Hybrid Perovskite Single-Crystal Nanowire Arrays for High-Performance Circularly Polarized Light Detection," *Advanced Science* 8 (2021): 2102065, https://doi.org/10.1002/advs.202102065.

17. J. Wu, X. Zhang, S. You, et al., "Low Detection Limit Circularly Polarized Light Detection Realized by Constructing Chiral Perovskite/Si Heterostructures," *Small* 19 (2023): 2302443, https://doi.org/10.1002/smll.202302443.

18. N. Y. Kim, J. Kyhm, H. Han, et al., "Chiroptical-Conjugated Polymer/Chiral Small Molecule Hybrid Thin Films for Circularly Polarized Light-Detecting Heterojunction Devices," *Advanced Functional Materials* 29 (2019): 1808668, https://doi.org/10.1002/adfm.201808668.

19. H. Lee, J. H. Hwang, S. H. Song, et al., "Chiroptical Synaptic Heterojunction Phototransistors Based on Self-Assembled Nanohelix of π-Conjugated Molecules for Direct Noise-Reduced Detection of Circularly Polarized Light," *Advanced Science* 10 (2023): 2304039, https://doi.org/10.1002/advs.202304039.

20. M. Mustaqeem, Z.-B. Jin, W. C. Tsai, et al., "Mechanically Tunable Circularly Polarized Flexible Spin Light Emitting Diodes," *Advanced Optical Materials* 13 (2025): 2500060, https://doi.org/10.1002/adom.202500060.

21. B. P. Bloom, V. Kiran, V. Varade, R. Naaman, and D. H. Waldeck, "Spin Selective Charge Transport Through Cysteine Capped CdSe Quantum Dots," *Nano Letters* 16 (2016): 4583, https://doi.org/10.1021/acs.nanolett.6b01880.

22. C. Wang, G. Li, Z. Dai, W. Tian, and L. Li, "Patterned Chiral Perovskite Film for Self-Driven Stokes Photodetectors," *Advanced Functional Materials* 34 (2024): 2316265, https://doi.org/10.1002/adfm.202316265.

23. T. Zhu, W. Weng, C. Ji, et al., "Chain-to-Layer Dimensionality Engineering of Chiral Hybrid Perovskites to Realize Passive Highly Circular-Polarization-Sensitive Photodetection," *Journal of the American Chemical Society* 144 (2022): 18062, https://doi.org/10.1021/jacs.2c07891.

24. Y. Zhao, X. Yin, Z. Gu, et al., "Interlayer Polymerization of 2D Chiral Perovskite Single-Crystal Films Toward High-Performance Flexible Circularly Polarized Light Detection," *Advanced Functional Materials* 33 (2023): 2306199, https://doi.org/10.1002/adfm.202306199.

25. A. Maiti and A. J. Pal, "Spin-Selective Charge Transport in Lead-Free Chiral Perovskites: The Key towards High-Anisotropy in Circularly-Polarized Light Detection," *Angewandte Chemie International Edition* 61 (2022): 202214161, https://doi.org/10.1002/anie.202214161.

26. M. Mustaqeem, S. Kamal, N. Ahmad, et al., "Chiral Metal-Organic Framework Based Spin-Polarized Flexible Photodetector with Ultrahigh Sensitivity," *Materials Today Nano* 21 (2023): 100303, https://doi.org/10.1016/j.mtnano.2023.100303.

27. M. Kim, M. Zhang, Y.-L. Zhu, et al., "A Neomorphic Protein Interface Catalyzes Covalent Inhibition of RASG12D Aspartic Acid in Tumors," *Science* 389 (2025): ads0239.

28. L. Liu, Y. Yang, L. Zhu, J. Zhang, K. Chen, and Z. Wei, "Chiral Non-Fullerene Acceptor Enriched Bulk Heterojunctions Enable High-Performance Near-Infrared Circularly Polarized Light Detection," *Small* 18 (2022): 2202941, https://doi.org/10.1002/smll.202202941.

29. H. Han, Y. J. Lee, J. Kyhm, et al., "High-Performance Circularly Polarized Light-Sensing Near-Infrared Organic Phototransistors for Optoelectronic Cryptographic Primitives," *Advanced Functional Materials* 30 (2020): 2006236, https://doi.org/10.1002/adfm.202006236.

30. L. Wan, R. Zhang, E. Cho, et al., "Sensitive Near-Infrared Circularly Polarized Light Detection via Non-Fullerene Acceptor Blends," *Nature Photonics* 17 (2023): 649, https://doi.org/10.1038/s41566-023-01230-z.

31. J. Kwon, J. B. Jeon, M. G. Lee, et al., "Enantioselective Se Lattices for Stable Chiroptoelectronic Processing Media," *Nature Communications* 16 (2025): 4134, https://doi.org/10.1038/s41467-025-59091-9.

32. H. Kim, R. M. Kim, S. D. Namgung, et al., "Ultrasensitive Near-Infrared Circularly Polarized Light Detection Using 3D Perovskite Embedded with Chiral Plasmonic Nanoparticles," *Advanced Science* 9 (2022): 2104598, https://doi.org/10.1002/advs.202104598.

33. J.-J. Lee, S.-J. Han, C. Choi, et al., "Polarization-Sensitive In-Sensor Computing in Chiral Organic Integrated 2D p-n Heterostructures for Mixed-Multimodal Image Processing," *Nature Communications* 16 (2025): 4624, https://doi.org/10.1038/s41467-025-59935-4.

34. Q. Guan, Z.-K. Zhu, H. Ye, et al., "Pyro-Phototronic Effect Induced Circularly Polarized Light Detection With a Broadband Response," *Advanced Science* 11 (2024): 2404403, https://doi.org/10.1002/advs.202404403.

35. S. D. Namgung, R. M. Kim, Y.-C. Lim, et al., "Circularly Polarized Light-Sensitive, Hot Electron Transistor with Chiral Plasmonic Nanoparticles," *Nature Communications* 13 (2022): 5081, https://doi.org/10.1038/s41467-022-32721-2.

36. S. Lee, J. Lee, H. R. Sim, C. So, and D. S. Chung, "Shortwave Infrared Organic Photodiodes Realized by Polaron Engineering," *Advanced Materials* 36 (2024): 2310250, https://doi.org/10.1002/adma.202310250.

37. S. Jee, M.-J. Si, J.-H. Choi, et al., "P-Type Colloidal InSb Quantum Dot Ink Enables III–V Group Bulk-Heterojunction Shortwave Infrared (SWIR) Photodetector," *Advanced Optical Materials* 12 (2024): 2303097, https://doi.org/10.1002/adom.202303097.

38. S. H. Kim, J. H. Ko, Y. J. Yoo, et al., "Single-Material, Near-Infrared Selective Absorber Based on Refractive Index-Tunable Tamm Plasmon Structure," *Advanced Optical Materials* 10 (2022): 2102388, https://doi.org/10.1002/adom.202102388.

39. L. Wang, W. Hao, B. Peng, J. Ren, and H. Li, "Nucleation-Controlled Crystallization of Chiral 2D Perovskite Single Crystal Thin Films for High-Sensitivity Circularly Polarized Light Detection," *Advanced Materials* 37 (2025): 2414199, https://doi.org/10.1002/adma.202414199.

40. J. Wu, T. Chang, Z. Yang, et al., "Magneto-Chiroptical Hybrid Perovskites with Anomalous Photovoltaic Effect for High-Performance Self-Driven Photodetectors," *Advanced Materials* 37 (2025): 2509074, https://doi.org/10.1002/adma.202509074.

41. C.-C. Fan, X.-B. Han, B.-D. Liang, et al., "Chiral Rashba Ferroelectrics for Circularly Polarized Light Detection," *Advanced Materials* 34 (2022): 2204119, https://doi.org/10.1002/adma.202204119.

42. Y. Peng, X. Liu, L. Li, et al., "Realization of vis–NIR Dual-Modal Circularly Polarized Light Detection in Chiral Perovskite Bulk Crystals," *Journal of the American Chemical Society* 143 (2021): 14077, https://doi.org/10.1021/jacs.1c07183.

43. W. Wu, X. Shang, Z. Xu, et al., "Toward Efficient Two-Photon Circularly Polarized Light Detection Through Cooperative Strategies in Chiral Quasi-2D Perovskites," *Advanced Science* 10 (2023): 2206070, https://doi.org/10.1002/advs.202206070.

44. L. Zhang, I. Song, J. Ahn, et al., "π-Extended Perylene Diimide Double-Heterohelicenes as Ambipolar Organic Semiconductors for Broadband Circularly Polarized Light Detection," *Nature Communications* 12 (2021): 142.

45. S. Ma, J. Ahn, and J. Moon, "Chiral Perovskites for Next-Generation Photonics: From Chirality Transfer to Chiroptical Activity," *Advanced Materials* 33 (2021): 2005760, https://doi.org/10.1002/adma.202005760.

46. J. Kang, D. Miyajima, T. Mori, Y. Inoue, Y. Itoh, and T. Aida, "A Rational Strategy for the Realization of Chain-Growth Supramolecular Polymerization," *Science* 347 (2015): 646, https://doi.org/10.1126/science.aaa4249.

47. N. Jeon, L. Kim, S. G. Choi, et al., "Self-Assembled Peptide-Gold Nanoparticle 1D Nanohybrids Functionalized with GHK Tripeptide for Enhanced Wound-Healing and Photothermal Therapy," *ACS Applied Materials & Interfaces* 17 (2025): 15080, https://doi.org/10.1021/acsami.4c21924.

48. S. D. Elliott, M. P. Moloney, and Y. K. Gun'ko, "Chiral Shells and Achiral Cores in CdS Quantum Dots," *Nano Letters* 8 (2008): 2452, https://doi.org/10.1021/nl801453g.

49. V. Mah and F. Jalilehvand, "Lead(II) Complex Formation with Glutathione," *Inorganic Chemistry* 51 (2012): 6285, https://doi.org/10.1021/ic300496t.

50. J. Kwon, J. B. Jeon, W. G. G. Júnior, et al., "Chiroferromagnetic Quantum Dots for Chiroptical Synapse (ChiropS)," *Advanced Materials* 37 (2025): 2415366, https://doi.org/10.1002/adma.202415366.

51. T. Liu, W. Shi, W. Tang, et al., "High Responsivity Circular Polarized Light Detectors based on Quasi Two-Dimensional Chiral Perovskite Films," *ACS Nano* 16 (2022): 2682, https://doi.org/10.1021/acsnano.1c09521.

52. S. Rajamani, D. Simeone, A. Pecora, et al., "Circularly Polarized Light Detection Through 3D Chiral Metasurface-Based Phototransistors," *Advanced Materials Technologies* 9 (2024): 2301250, https://doi.org/10.1002/admt.202301250.

53. Q. Wang, H. Zhu, Y. Tan, et al., "Spin Quantum Dot Light-Emitting Diodes Enabled by 2D Chiral Perovskite with Spin-Dependent Carrier Transport," *Advanced Materials* 36 (2024): 2305604, https://doi.org/10.1002/adma.202305604.

54. Y.-H. Kim, Y. Zhai, H. Lu, et al., "Chiral-Induced Spin Selectivity Enables a Room-Temperature Spin Light-Emitting Diode," *Science* 371 (2021): 1129, https://doi.org/10.1126/science.abf5291.

55. M. Mustaqeem, P.-T. Chou, S. Kamal, et al., "Solution-Processed and Room-Temperature Spin Light-Emitting Diode Based on Quantum Dots/Chiral Metal-Organic Framework Heterostructure," *Advanced Functional Materials* 33 (2023): 2213587, https://doi.org/10.1002/adfm.202213587.

56. L. Yang, Y. Gao, Z. Wang, L. Yang, and M. Shao, "Spin Detector for Panchromatic Circularly Polarized Light Detection," *Nature Communications* 16 (2025): 4161, https://doi.org/10.1038/s41467-025-59287-z.

57. B. P. Bloom, Y. Paltiel, R. Naaman, and D. H. Waldeck, "Chiral Induced Spin Selectivity," *Chemical Reviews* 124 (2024): 1950, https://doi.org/10.1021/acs.chemrev.3c00661.

58. K. Chae, N. A. R. C. Mohamad, J. Kim, et al., "The Promise of Chiral Electrocatalysis for Efficient and Sustainable Energy Conversion and Storage: A Comprehensive Review of the CISS Effect and Future Directions," *Chemical Society Reviews* 53 (2024): 9029, https://doi.org/10.1039/D3CS00316G.

59. S. He, W. Lin, D. Yu, et al., "Perovskite Spin Light-Emitting Diodes with Simultaneously High Electroluminescence Dissymmetry and High External Quantum Efficiency," *Nature Communications* 16 (2025): 2201, https://doi.org/10.1038/s41467-025-57472-8.

60. Y. S. Jeon, E. Jeong, S. W. Im, et al., "Spin-Selective Transport through Chiral Ferromagnetic Nanohelices," *Science* 389 (2025): 1031, https://doi.org/10.1126/science.adx5963.

61. Z. Fu, L. Zhou, Y. Yin, et al., "Direct Photo-Patterning of Efficient and Stable Quantum Dot Light-Emitting Diodes via Light-Triggered, Carbocation-Enabled Ligand Stripping," *Nano Letters* 23 (2023): 2000–2008.

62. L. Qian, Y. Zheng, J. Xue, and P. H. Holloway, "Stable and Efficient Quantum-Dot Light-Emitting Diodes Based on Solution-Processed Multilayer Structures," *Nature Photonics* 5 (2011): 543, https://doi.org/10.1038/nphoton.2011.171.

63. S. Li, J. H. Jang, W. Chung, et al., "Ultrathin Self-Powered Heavy-Metal-Free Cu–In–Se Quantum Dot Photodetectors for Wearable Health Monitoring," *ACS Nano* 17 (2023): 20013, https://doi.org/10.1021/acsnano.3c05178.

64. V. A. Kuznetsova, E. Mates-Torres, N. Prochukhan, et al., "Effect of Chiral Ligand Concentration and Binding Mode on Chiroptical Activity of CdSe/CdS Quantum Dots," *ACS Nano* 13 (2019): 13560, https://doi.org/10.1021/acsnano.9b07513.

65. F. Purcell-Milton, A. K. Visheratina, V. A. Kuznetsova, A. Ryan, A. O. Orlova, and Y. K. Gun'ko, "Impact of Shell Thickness on Photoluminescence and Optical Activity in Chiral CdSe/CdS Core/Shell Quantum Dots," *ACS Nano* 11 (2017): 9207, https://doi.org/10.1021/acsnano.7b04199.

66. A. B. Moshe, D. Szwarcman, and G. Markovich, "Size Dependence of Chiroptical Activity in Colloidal Quantum Dots," *ACS Nano* 5 (2011): 9034, https://doi.org/10.1021/nn203234b.

67. T. Kurihara, Y. Noda, and K. Takegoshi, "Capping Structure of Ligand–Cysteine on CdSe Magic-Sized Clusters," *ACS Omega* 4 (2019): 3476, https://doi.org/10.1021/acsomega.8b02752.

68. P. Rodríguez-Zamora, C. A. Cordero-Silis, G. R. Garza-Ramos, et al., "Effect of the Metal–Ligand Interface on the Chiroptical Activity of Cysteine-Protected Nanoparticles," *Small* 17 (2021): 2004288, https://doi.org/10.1002/smll.202004288.

69. Y. Cozzens, P. Wang, and J. E. Whitten, "Adsorption of l -Cysteine and Cysteamine on Zinc Oxide Nanoparticles," *Langmuir* 40 (2024): 23538, https://doi.org/10.1021/acs.langmuir.4c03497.

70. J. Ge, T. Yin, H. Zhang, et al., "Photo-Crosslinking of Doped Magic-Sized Nanoclusters for the Construction of Enhanced Electrochemiluminescence Biosensors," *Chemical Science* 16 (2025): 3671, https://doi.org/10.1039/D4SC07800D.

71. M. Ai, L. Pan, C. Shi, et al., "Spin Selection in Atomic-Level Chiral Metal Oxide for Photocatalysis," *Nature Communications* 14 (2023): 4562, https://doi.org/10.1038/s41467-023-40367-x.

72. Q. Gu, J. Zha, C. Chen, et al., "Constructing Chiral Covalent-Organic Frameworks for Circularly Polarized Light Detection," *Advanced Materials* 36 (2024): 2306414, https://doi.org/10.1002/adma.202306414.

73. A. Alexandrov, M. Zvaigzne, D. Lypenko, I. Nabiev, and P. Samokhvalov, "Al-, Ga-, Mg-, or Li-Doped Zinc Oxide Nanoparticles as Electron Transport Layers for Quantum Dot Light-Emitting Diodes," *Scientific Reports* 10 (2020): 7496, https://doi.org/10.1038/s41598-020-64263-2.

74. D. M. Kroupa, M. Vörös, N. P. Brawand, et al., "Tuning Colloidal Quantum Dot Band Edge Positions through Solution-Phase Surface Chemistry Modification," *Nature Communications* 8 (2017): 15257, https://doi.org/10.1038/ncomms15257.

75. B. R. Lee, E. D. Jung, Y. S. Nam, et al., "Amine-Based Polar Solvent Treatment for Highly Efficient Inverted Polymer Solar Cells," *Advanced Materials* 26 (2014): 494, https://doi.org/10.1002/adma.201302991.

76. S. Li, S.-M. Jung, W. Chung, et al., "Defect Engineering of Ternary Cu–In–Se Quantum Dots for Boosting Photoelectrochemical Hydrogen Generation," *Carbon Energy* 5: 384, https://doi.org/10.1002/cey2.384.

77. T. Fujita, K. Morimoto, H. Kiyama, et al., "Angular Momentum Transfer from Photon Polarization to an Electron Spin in a Gate-Defined Quantum Dot," *Nature Communications* 10 (2019): 2991, https://doi.org/10.1038/s41467-019-10939-x.

78. F. Zheng, L. Z. Tan, S. Liu, and A. M. Rappe, "Rashba Spin–Orbit Coupling Enhanced Carrier Lifetime in $CH_3NH_3PbI_3$," *Nano Letters* 15 (2015): 7794, https://doi.org/10.1021/acs.nanolett.5b01854.

79. M. Syperek, D. R. Yakovlev, I. A. Yugova, et al., "Long-Lived Electron Spin Coherence in CdSe/Zn(S,Se) Self-Assembled Quantum Dots," *Physical Review B* 84 (2011): 085304, https://doi.org/10.1103/PhysRevB.84.085304.

80. D. H. Feng, X. Li, T. Q. Jia, X. Q. Pan, and Z. R. Sun, "Long-Lived, Room-Temperature Electron Spin Coherence in Colloidal CdS Quantum Dots," *Applied Physics Letters* 100 (2012): 122406, https://doi.org/10.1063/1.3696069.

81. M. Szymura, M. Duda, M. Karpińska, et al., "Low-Temperature Photoluminescence Dynamics Reveal the Mechanism of Light Emission by Colloidal CuInS 2 Quantum Dots," *The Journal of Physical Chemistry C* 127 (2023): 6768, https://doi.org/10.1021/acs.jpcc.3c00536.

82. S. Watanabe, K. Ando, K. Kang, et al., "Polaron Spin Current Transport in Organic Semiconductors," *Nature Physics* 10 (2014): 308, https://doi.org/10.1038/nphys2901.

83. J. Zhang, R. W. Crisp, J. Gao, D. M. Kroupa, M. C. Beard, and J. M. Luther, "Synthetic Conditions for High-Accuracy Size Control of PbS Quantum Dots," *The Journal of Physical Chemistry Letters* 6 (2015): 1830, https://doi.org/10.1021/acs.jpclett.5b00689.

84. R. Hu, X. Lu, X. Hao, and W. Qin, "An Organic Chiroptical Detector Favoring Circularly Polarized Light Detection From Near-Infrared to Ultraviolet and Magnetic-Field-Amplifying Dissymmetry in Detectivity," *Advanced Materials* 35 (2023): 2211935, https://doi.org/10.1002/adma.202211935.

85. L. Li, J. Wang, L. Kang, et al., "Monolithic Full-Stokes Near-Infrared Polarimetry with Chiral Plasmonic Metasurface Integrated Graphene–Silicon Photodetector," *ACS Nano* 14 (2020): 16634, https://doi.org/10.1021/acsnano.0c00724.

86. W. Li, Z. J. Coppens, L. V. Besteiro, W. Wang, A. O. Govorov, and J. Valentine, "Circularly Polarized Light Detection with Hot Electrons in Chiral Plasmonic Metamaterials," *Nature Communications* 6 (2015): 8379, https://doi.org/10.1038/ncomms9379.

87. Y. Wang, H. Wu, C. Rodà, et al., "Shortwave Infrared Light Detection and Ranging Using Silver Telluride Quantum Dots," *Advanced Materials* 37 (2025): 2500977, https://doi.org/10.1002/adma.202500977.

88. Y. Wang, L. Peng, J. Schreier, et al., "Silver Telluride Colloidal Quantum Dot Infrared Photodetectors and Image Sensors," *Nature Photonics* 18 (2024): 236, https://doi.org/10.1038/s41566-023-01345-3.

89. Y. Ahn, S. Y. Eom, G. Kim, et al., "Silver Telluride Colloidal Quantum Dot Solid for Fast Extended Shortwave Infrared Photodetector," *Advanced Science* 11 (2024): 2407453, https://doi.org/10.1002/advs.202407453.

90. J. A. Lee, I. S. Lee, D. Kang, et al., "Chemical Reactivity-Controlled Synthesis of Silver Chalcogenide Colloidal Quantum Dots for Efficient Shortwave Infrared Photodetectors," *Small* 21 (2025): 2412420, https://doi.org/10.1002/smll.202412420.

91. J. Liu, P. Liu, T. Shi, et al., "Flexible and Broadband Colloidal Quantum Dots Photodiode Array for Pixel-Level X-ray to Near-Infrared Image Fusion," *Nature Communications* 14 (2023): 5352, https://doi.org/10.1038/s41467-023-40620-3.

92. Y.-H. Deng, C. Pang, E. Kheradmand, et al., "Short-Wave Infrared Colloidal QD Photodetector with Nanosecond Response Times Enabled by Ultrathin Absorber Layers," *Advanced Materials* 36 (2024): 2402002, https://doi.org/10.1002/adma.202402002.

93. U. Tohgha, K. K. Deol, A. G. Porter, et al., "Ligand Induced Circular Dichroism and Circularly Polarized Luminescence in CdSe Quantum Dots," *ACS Nano* 7 (2013): 11094, https://doi.org/10.1021/nn404832f.

Supporting Information

Additional supporting information can be found online in the Supporting Information section.

Supporting File 1: adma72224-sup-0001-SuppMat.pdf.